



Differentiation in corrosion performance of alumina forming alloys in alkali carbonate melts

Downloaded from: <https://research.chalmers.se>, 2025-12-05 04:39 UTC

Citation for the original published paper (version of record):

Mohamedin, E., Strach, M., Olovsjö, J. et al (2021). Differentiation in corrosion performance of alumina forming alloys in alkali carbonate melts. Corrosion Science, 192.
<http://dx.doi.org/10.1016/j.corsci.2021.109857>

N.B. When citing this work, cite the original published paper.



Differentiation in corrosion performance of alumina forming alloys in alkali carbonate melts

Esraa Hamdy^{a,*}, Michal Strach^b, Johanna Nockert Olovssjö^c, Christine Geers^a

^a Energy and Materials, Chemistry and Chemical Engineering, Chalmers University of Technology, Gothenburg, Sweden

^b Chalmers Materials Analysis Laboratory, Physics, Chalmers University of Technology, Gothenburg, Sweden

^c Kanthal AB, Hallstahammar, Sweden

ARTICLE INFO

Keywords:

Lithium aluminate
Alumina forming alloys
Molten carbonates
High temperature corrosion
Phase transition

ABSTRACT

Alkali carbonate melts are promising high temperature thermal storage media. In this work five alumina forming alloys have been exposed to a ternary LiNaK carbonate melt and CO₂ at 800 °C. The corrosion propagation was found to depend on the formation of a slow-growing LiAlO₂ scale. Furthermore, the two polymorphs contributing to the LiAlO₂ phase were monitored for up to 1000 h: a dense α-LiAlO₂ scale and γ-LiAlO₂ crystallites. We suggest a growth stress assisted formation of α-LiAlO₂ relaxing into the outwards growing γ-LiAlO₂ phase. This implies a deceleration of the α-LiAlO₂ scale growth towards a steady state-thickness.

1. Introduction

New generations of climate-neutral energy technologies, such as concentrated solar power (CSP) with thermal storage capacities, surpass current temperature limitations by utilising high temperature heat transport and storage media with superior thermal stability [1–5]. While reaching for increased energy conversion efficiency and grid stability, material challenges due to high temperature corrosion risks lack data on long-term performance, especially when it comes to selected molten salt mixtures in contact with metal components. These eutectic melts comprise commonly ternary alkali carbonates or binary chloride mixtures. The first pilot plant operating with ternary carbonates comprising lithium-, sodium, and potassium carbonates (LiNaK) operates at 700 °C [1].

Metal components are made of high temperature resistant alloys providing structural strength as well as containment of the salt, while growing a passivating oxide scale at the surface, preventing corrosion by molten species. Formation and slow growth of a passivating oxide scale are crucial for alloy components' overall performance and, subsequently, the entire power plant. Chromium oxide on stainless steels and aluminium oxide on ferritic alumina forming alloys are common candidates to establish a high temperature corrosion protection in next-generation thermal storages utilising alkali carbonates at 700 °C or higher. However, a chromium oxide scale has proven insufficient to protect an alloy against internal oxidation and rapid carburisation,

causing material embrittlement [6,7]. On the other hand, studies on alumina forming alloys showed that slow-growing alkali aluminate scales do not permeate carbon [8,9]. In this aspect, alumina forming alloys are superior to all chromia forming steels. In a previous study [7], we report specifically on the time-resolved performance of the alumina forming Kanthal® APMT at 800 °C immersed in LiNaK carbonates. Lithium ions have shown to be the predominant alkali species incorporated into oxides growing on high-temperature alloys [7,10,11]. After 72 h, the surface was covered by an α-lithium aluminate layer. After a few hundred hours, larger crystallites have been observed and identified as γ-lithium aluminate.

In the spirit of identifying the higher temperature operation limit, this research was conducted at 800 °C.

The solid-state synthesis of LiAlO₂ and characterisation of its two polymorphs α and γ has been published by Lehmann and Hasselbarth in 1961. In air, the low-temperature modification, α-LiAlO₂, transforms into γ-LiAlO₂ at 600 °C or higher [12]. In several studies, reacting lithium carbonate with alumina powder in different environments revealed that the upper-temperature limit for α-LiAlO₂ formation is in the range of 747–777 °C [13–16].

Evans et al. introduced in 1978 a concept for the stress assisted formation of a duplex oxide scale comprising two polymorphs, i.e., tetragonal and monoclinic zirconia on zircaloy-2 [17]. In the present study, the same concept is adopted to express the growth of both α- and γ-LiAlO₂ at 800 °C. In Evans's case, a stress stabilised tetragonal zirconia

* Corresponding author.

E-mail address: esraah@chalmers.se (E. Hamdy).

<https://doi.org/10.1016/j.corsci.2021.109857>

Received 19 July 2021; Received in revised form 13 September 2021; Accepted 14 September 2021

Available online 20 September 2021

0010-938X/© 2021 The Author(s). Published by Elsevier Ltd. This is an open access article under the CC BY license (<http://creativecommons.org/licenses/by/4.0/>).

morphology forms at the metal/oxide interface under compressive stress until relaxing into a monoclinic lattice. The magnitude of the compressive stress allows tetragonal ZrO_2 to form at a significantly lower temperature than its ambient pressure phase transition point, as indicated in the T-P-phase diagram [18]. Detailed investigations are still regularly published to understand and predict a limiting scale thickness [19,20], also referred to as steady-state thickness, due to its technological importance for nuclear applications [19]. Evans et al. emphasised in 1978 that the concept of a stress stabilised inner oxide scale is universal under the condition of two possible polymorphs. We believe that the α - to γ - LiAlO_2 transformation is one of these examples, which leads to the assumption of a limiting steady-state thickness of the α - LiAlO_2 inner oxide layer.

It should be mentioned that the density of γ - LiAlO_2 is 25% lower compared to α - LiAlO_2 . The crystal structure visualisation in Fig. 1 [21, 22] highlights the layered packing of lithium and aluminium ion polyhedrons along the c-axis for α - LiAlO_2 , while γ - LiAlO_2 comprises alternating Li/Al tetrahedrons [22].

In this study, the corrosion processes on the alumina forming alloys Kanthal® APMT, Kanthal® AF, Nikrothal® PM58, and two newly developed alloys, Fe10Cr4Al base, in LiNaK carbonate melt at 800 °C will be described.

2. Experimental

Specimens of five alumina forming alloys have been prepared and investigated in this study. The alloys have relatively similar aluminium content. The nominal compositions of Kanthal® AF and Kanthal® APMT are almost identical, Fe20Cr5Al however, the latter differs in Mo and Mn content (Table 1.).

The newly developed Kanthal® EF100 and 101, Fe10Cr4Al, differ in Si content. Nikrothal® PM58 is an alumina-forming austenitic alloy.

A salt mixture of 32.1 wt% Li_2CO_3 , 33.4 wt% Na_2CO_3 and - 34.5 wt% K_2CO_3 was prepared and have been purchased from VWR chemicals (99.0%), EMSURE anhydrous (99.9%), and ThermoFisher Scientific (99.8%), respectively.

The salt preparation method, chemical composition and concentration of each salt impurities are stated in [23]. A unique setup was built to provide a full immersion of coupons into the salt melt during exposures. A detailed description of the setup built is given in a previous publication [23]. The isothermal exposures were conducted at 800 ± 5 °C under flowing CO_2 . Upon each experiment, two duplicate samples are produced and are differently treated, as will be discussed further, depending on the characterisation technique. Each exposure was repeated at least two times for each material.

Metal coupons of initial measurements $15 \times 15 \times 2$ mm were prepared to a mirror-like finish (1 μm diamond polish). The polished samples were thoroughly cleaned and dried, then immersed in the prepared salt mixture. Detailed procedure of metal coupons preparation is provided in a former publication [23].

2.1. Post-exposure surface analysis

After exposure, samples were differently treated based on the type of investigations required. For example, samples subjected to surface investigations, X-ray diffraction (XRD) analysis, and mass change measurements have been rinsed with water by an ultrasonic cleaner at room temperature, see [23]. After weighing the washed samples, surface investigations were conducted by scanning electron microscopy (SEM) and energy-dispersive X-ray spectroscopy (EDX) using a JEOL JSM-7800F Prime or Phenom ProX Desktop SEM with an EDX detector. The Siemens D5000 powder diffractometer equipped with a Cu source, a secondary Si monochromator, and a point detector with grazing-incidence geometry was used for XRD surface analysis. Li containing species were exclusively detectable through XRD.

Rietveld refinement on the acquired XRD patterns was performed using the TOPAS V6 software. Rietveld refinement on the phases included zero-error corrections, polarisation factor, a fundamental parameters approach for instrumental profile simulation, preferred orientation correction based on spherical harmonics, corresponding emission profile, and polynomial simulated background. The structures used in the refinement were trigonal R-3 M for the α - LiAlO_2 phase, tetragonal P41212 for the γ - LiAlO_2 phase, and cubic Im-3 m for the FeCrAl substrate phase.

It has to be noted that the applied model does not include absorption effects in the layered structure. Signal from the inner oxide layer will be decreased by the growing outer scale, affecting the measured peak intensities. In addition, the penetration depth in the used grazing incidence geometry cannot be determined without exact incidence angle values and densities (packing) of the probed layers. Hence, the obtained phase fractions provide only qualitative insights and require additional parameters obtained by microscopic inspection of cross-sections.

2.2. Post-exposure cross-section analysis

For cross-sectional investigations, samples were not rinsed. After pouring out the melt, a thin salt film stays on the top of the sample. Cross-sections of the exposed samples were prepared via dry cutting with a low-speed diamond saw, followed by broad ion beam (BIB) milling with a Leica TIC 3X instrument.

3. Results

In this section, the corrosion behaviour of the selected alumina forming alloys will be discussed based on mass change measurements, XRD and Rietveld analysis, and microscopic investigations (surface morphology and cross-sectional analysis).

3.1. Mass change measurements of alumina forming alloys exposed to alkali carbonate melts

Corrosion performance is evaluated quantitatively by measuring the

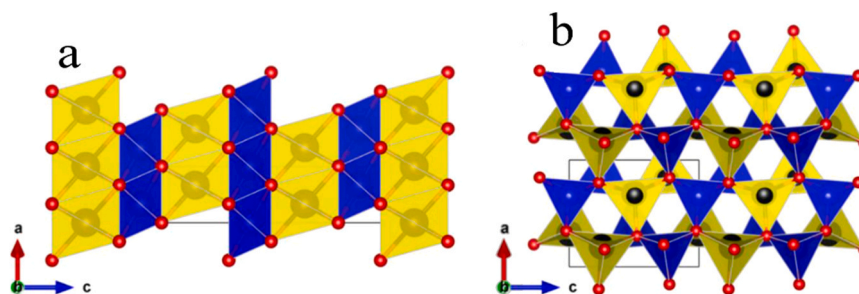


Fig. 1. Three-dimensional polyhedral visualisation of a) α - LiAlO_2 and b) γ - LiAlO_2 crystal structures, where red, yellow and blue spheres represent oxygen, lithium and aluminium atoms [21,22].

Table 1
Nominal alloy compositions.

Alloy	Fe	Ni	Cr	Al	Si	Mn	Mo	Others
Kanthal® APMT	balance	X	21	5	0.7	0.4	3	RE; C 0.08
Kanthal® AF	balance	X	21	5.3	0.7	X	X	RE; C 0.08
Kanthal® EF101	balance	< 0.5	11–14	3.2–4.2	1.2	< 0.7	X	RE; C 0.08
Kanthal® EF100	balance	< 0.5	9.5–13	3.8–4.2	< 0.5	< 0.7	X	RE; C 0.08
Nikrothal® PM58	18	Balance	19	5	0.4	X	X	RE

mass change of the samples after being rinsed with water [23]. Due to the rinsing procedure, the soluble oxide species are dissolved; therefore, the mass change values must be interpreted cautiously. LiAlO_2 was not found to dissolve by this procedure. Nevertheless, the mass change plot, besides other analyses, can give an indication on the scale formation and growth kinetics. As shown in Fig. 2, all alumina forming alloys have shown relatively similar mass gain values. After 72 h, the mass gain obtained shows that Kanthal® EF 101 has the lowest mass gain, followed by Kanthal® APMT and Kanthal® AF, which have relatively similar mass change values; Nikrothal® PM58 has the highest mass gain, while the Kanthal® EF 100 has shown a mass loss.

The mass change data will be used in Table 2. to estimate α/γ - LiAlO_2 phase transformation ratios, in comparison to the Rietveld data.

3.2. "Normal" formation and transformation of LiAlO_2

In this study, the selected alloys will be categorised into two groups based on their formation and transformation behaviour of LiAlO_2 : i) "normal" and ii) "deviating". The "normal" formation and transformation of LiAlO_2 is incorporating no ternary cationic species from the alloy and is therefore chemically very similar to the synthesis products already described by Lehmann and Hasselbarth [12]. The "deviating" behaviour described in the next chapter involves at least one more metal ion in the scale formation. Fig. 3. shows the XRD patterns of the Kanthal® EF 101 after exposure to alkali carbonate melts at 800 °C. After short-term exposure (72 h and 168 h), only one phase of LiAlO_2 has been identified, i.e. α - LiAlO_2 . After longer exposures (500 h and 1000 h), another lithium aluminate phase, γ - LiAlO_2 emerged. These findings are similar for Kanthal® APMT and Kanthal® AF. In Table 2. the α/γ LiAlO_2 phase ratios are quantified by Rietveld analysis.

Fig. 4. displays the relatively similar surface morphology of Kanthal® APMT, Kanthal® AF, and Kanthal® EF 101. After short-term exposure (72/168 h), small crystals, identified as α - LiAlO_2 , completely covered the surface. After longer exposure times (500 h/1000 h), the larger γ - LiAlO_2 phase started to emerge.

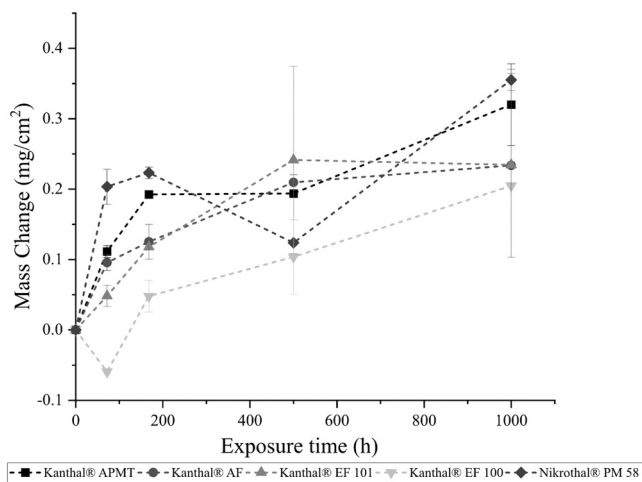


Fig. 2. Overall mass change behaviour of the selected alumina forming alloys immersed in alkali carbonate at 800 °C after different exposure times.

Fig. 5 shows an example of the characteristic double-layer structure composed of a compact inner α - LiAlO_2 scale and outer γ - LiAlO_2 crystals, on Kanthal® EF 101. The average scale thicknesses of the "normal" behaving LiAlO_2 forming alloys have been measured and tabulated in Table 2. Kanthal® APMT shows the thickest α - LiAlO_2 scale among the "normal" behaving alloys.

The measured mass gain, $\Delta m(\text{measured})$, for the "normal" LiAlO_2 formers represents the uptake of lithium and oxygen into the scale. The amount of substance (n) for LiAlO_2 is obtained by correcting the measured mass gain for the aluminium contribution from the alloy (41% of the molar mass M_{LiAlO_2}) divided by the total M_{LiAlO_2} , Eq. 1. The α - LiAlO_2 phase in the "normal" scenario forms a rather homogeneous scale at the surface with a mean thickness $X(\alpha)$. The mean thickness $X(\alpha)$ derived from cross-sectional analyses multiplied by sample area and theoretical density of α - LiAlO_2 from the crystallographic database [22] allows us to determine an approximate total mass of α - LiAlO_2 and consequently an amount of substance, $n(\alpha)$.

$$n(\text{LiAlO}_2 \text{ total}) = n(\alpha) + n(\gamma) = \frac{\Delta m(\text{measured}) \cdot 1.69}{M(\text{LiAlO}_2)} \quad (1)$$

For each sample of the "normal" LiAlO_2 formers, the α/γ -phase ratio was determined using Eq. 1, combining gravimetry and microscopy. Rietveld refinement for each powder diffractogram has been used as an alternative quantification of α/γ - LiAlO_2 ratios for comparison.

The α/γ phase ratios derived by Rietveld refinement contain information on the increasing coverage of the sample surfaces by γ - LiAlO_2 . The ratios determined by combined microscopy and gravimetric measurements allow for a quantification of the α - LiAlO_2 scale contribution to the total mass gain. All values are tabulated in Table 2. It is noteworthy that the mass gain and scale thickness used in the calculations are for two different coupons. However, they have been exposed simultaneously under the same conditions.

Plotting scale thicknesses and the α/γ -phase ratio (Rietveld) in Fig. 6. reveals the growth of α - and γ - LiAlO_2 phase over time. It is noteworthy to point out that the α/γ ratios derived by Rietveld analysis plotted in Fig. 6 seem to indicate a deceleration or even reducing γ - LiAlO_2 fraction after 500 h for Kanthal APMT and Kanthal EF101, while the average thickness is steadily increasing. The top view images in Fig. 4. show that the individual γ - LiAlO_2 crystals grow significantly with time but the overall number of nucleation sites does not increase. This can have an effect on the Rietveld phase fraction slope in Fig. 6. The rapid increase of size and phase fraction of γ - LiAlO_2 may lead to Al depletion in the bulk alloy. Thus, line scan analysis has been performed on all 1000 h exposure samples and did not substantiate that concern (Fig. 5.d). The α - LiAlO_2 scale growth decelerates over time.

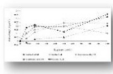
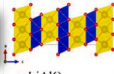
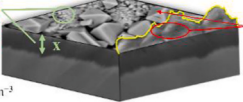
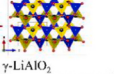
Summarising the observations for the "normally" behaving LiAlO_2 forming alloys, minor deviations can be found for each parameter, i.e., as surface roughness, crystals size and scale thickness.

3.3. "Deviating" formation and transformation of LiAlO_2

The corrosion behaviour of the Kanthal® EF 100 and Nikrothal® PM 58 deviates from the "normal" α - LiAlO_2 forming alloys, particularly after short-term exposures. In the case of Kanthal® EF 100, the alloy surface was completely covered with LiFeO_2 crystals after 72 h, as shown in Fig. 7.c and confirmed with XRD, Fig. 8. After 168 h, however, all traces

Table 2

Mean scale thicknesses (X) for α - and γ -LiAlO₂, mass change Δm , gravimetrically and microscopically derived α/γ -phase ratio (calc. Eq. 1) and Rietveld derived phase ratios (α to γ % Rietveld). The n.a. (not available) error data in the table is attributable to duplicate sample loss in the repeated experiment due to alumina crucible breakdown during cooling.

<div><div><p>Δm (mg/cm²)</p></div><div><p>α-LiAlO₂ $\rho_{\alpha\text{-LiAlO}_2} = 3.40 \text{ g}\cdot\text{cm}^{-3}$</p></div><div><p>γ-LiAlO₂ $\rho_{\gamma\text{-LiAlO}_2} = 2.59 \text{ g}\cdot\text{cm}^{-3}$</p></div><div><p>α/γ % Rietveld refinement</p></div></div>					
Exposure Time	Δm (mg/cm ²)	X_{measured} (μm)	α to γ % calc.	α to γ % Rietveld	
Kanthal® APMT					
72 h	α	0.11±0.008	0.30 (Max 0.6)	97.33	100
	γ		-	2.67	0
168 h	α	0.19±n.a	0.75 (Max 2.4)	77.05	100
	γ		-	22.95	0
500 h	α	0.19±0.002	0.95 (Max 3.2)	96.40	63.9 ± 0.9
	γ		1.60 (Max 2.3)	3.60	36.1± 0.9
1000 h	α	0.32±0.06	1.80 (Max 3.2)	93.67	78.1 ± 1.1
	γ		5.2 (Max 8.8)	6.33	21.9± 1.1
Kanthal® AF					
72 h	α	0.10±0.01	0.45 (Max 0.7)	93.79	100
	γ		-	6.21	0
168 h	α	0.13±0.02	0.5 (Max 0.7)	65.93	85.5±2.5
	γ		0.42 (Max 0.6)	34.07	14.5±1.9
500 h	α	0.21±0.01	0.6 (Max 0.7)	47.96	70±1
	γ		0.85 (Max 4.4)	52.04	30±1
1000 h	α	0.23±0.13	1.13 (Max 1.8)	33.59	9.8±2.5
	γ		3.0 (Max 4.3)	66.41	90.2±2.4
Kanthal® EF 101					
72 h	α	0.05±0.01	0.45 (Max 1.2)		100
	γ		-		0
168 h	α	0.12±n.a	0.47 (Max 0.6)	75.84	64±0.9
	γ		0.75 (Max 1.25)	24.16	36±0.9
500 h	α	0.24±0.13	0.52 (Max 0.7)	27.13	18±5
	γ		1.4 (Max 2.7)	72.87	82±5
1000 h	α	0.23±n.a	0.6 (Max 1.1)	51.06	20.2±3.8
	γ		1.7 (Max 3.5)	48.94	79.8±3.3

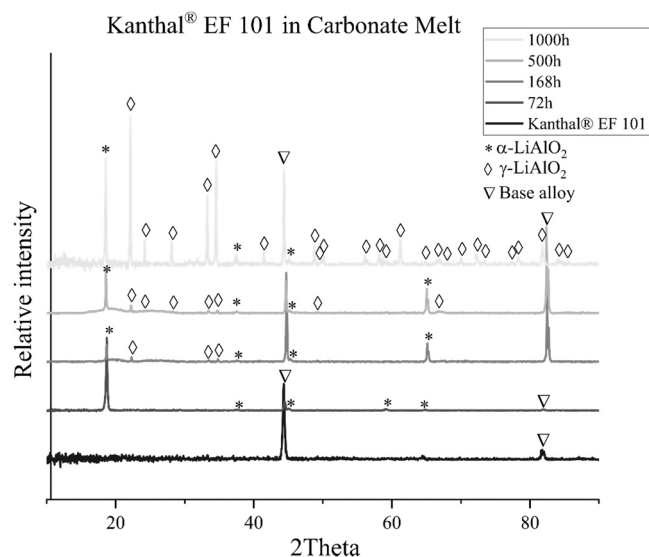


Fig. 3. XRD patterns of Kanthal® EF 101 after exposure to alkali carbonates in CO₂ at 800 °C for 72 h, 168 h, 500 h and 1000 h.

of LiFeO₂ have disappeared due to dissolution into the carbonate melt (Fig. 7d and g). This observation is in agreement with the observed mass loss, cf. Fig. 2. Instead, small crystals of α -LiAlO₂ are formed. Furthermore, after longer exposure times (500 h/1000 h), γ -LiAlO₂ crystals started to grow similarly to the "normally" behaving alloys. Due to the initial mass loss induced by the transient α -LiFeO₂, the coupled gravimetric/microscopic determination of the α/γ -LiAlO₂ phase ratio via Eq. 1 was not applicable here. However, α/γ -LiAlO₂ phase ratios have been obtained by Rietveld refinement of the XRD patterns obtained after 168 h, 500 h and 1000 h exposures. The Rietveld data and mean scale thicknesses are shown for comparison in Fig. 6. Indeed, the slow growth of the thin α -LiAlO₂ scale and scarce nucleation of γ -LiAlO₂ crystallites at the surface lead us to classify Kanthal® EF 100 as one of the "normally" behaving LiAlO₂ forming alloys after overcoming a deviating early stage.

At 800 °C the austenitic alloy Nikrothal® PM58 forms Li(Cr,Al)O₂ in contrast to the protective α -LiAlO₂ scale that has been reported for exposures at 750 °C [24]. Fig. 9. shows XRD and microscopic analysis results of Nikrothal® PM58 after exposure to alkali carbonate melts for at least 1000 h. Cross-section and EDX analyses revealed that Nikrothal® PM58 developed pegs in the suboxide zone filled with mainly Li(Cr,Al)O₂ and some fractions of aluminium enriched scale as well as nickel and iron-rich particles. In Fig. 9.c-e, point analysis on the surface reveal that Fe and Ni particles have been transported to the oxide/melt interface

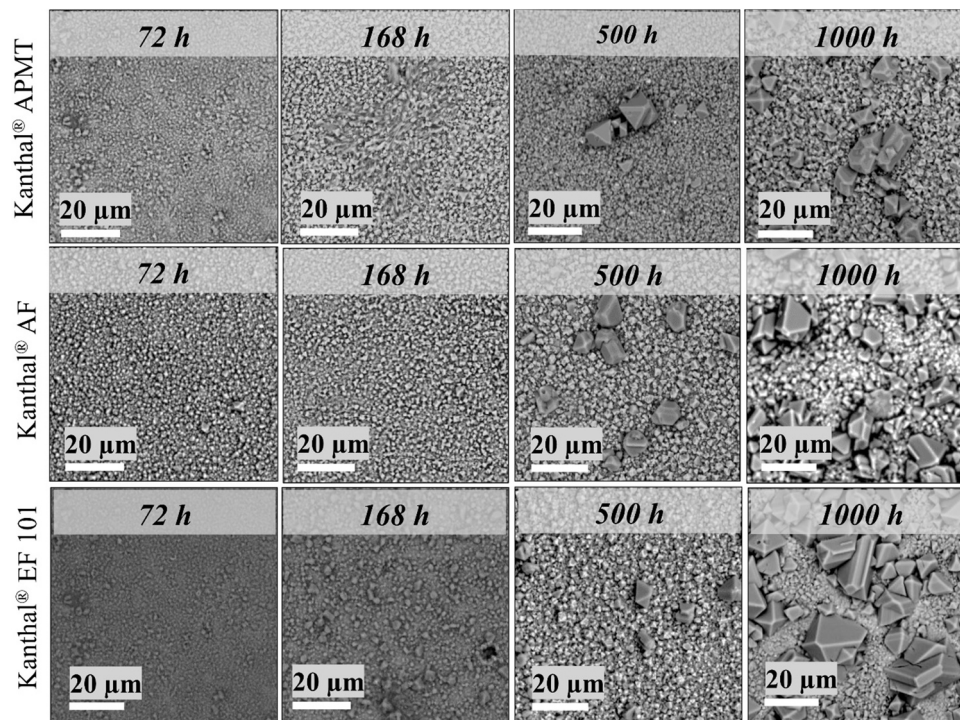


Fig. 4. Top view electron microscopic images for "normal behaving alloys" only LiAlO_2 species exposed to carbonate melts at 800 °C after different exposure times. Larger crystals present $\gamma\text{-LiAlO}_2$, small crystals are attributed to $\alpha\text{-LiAlO}_2$.

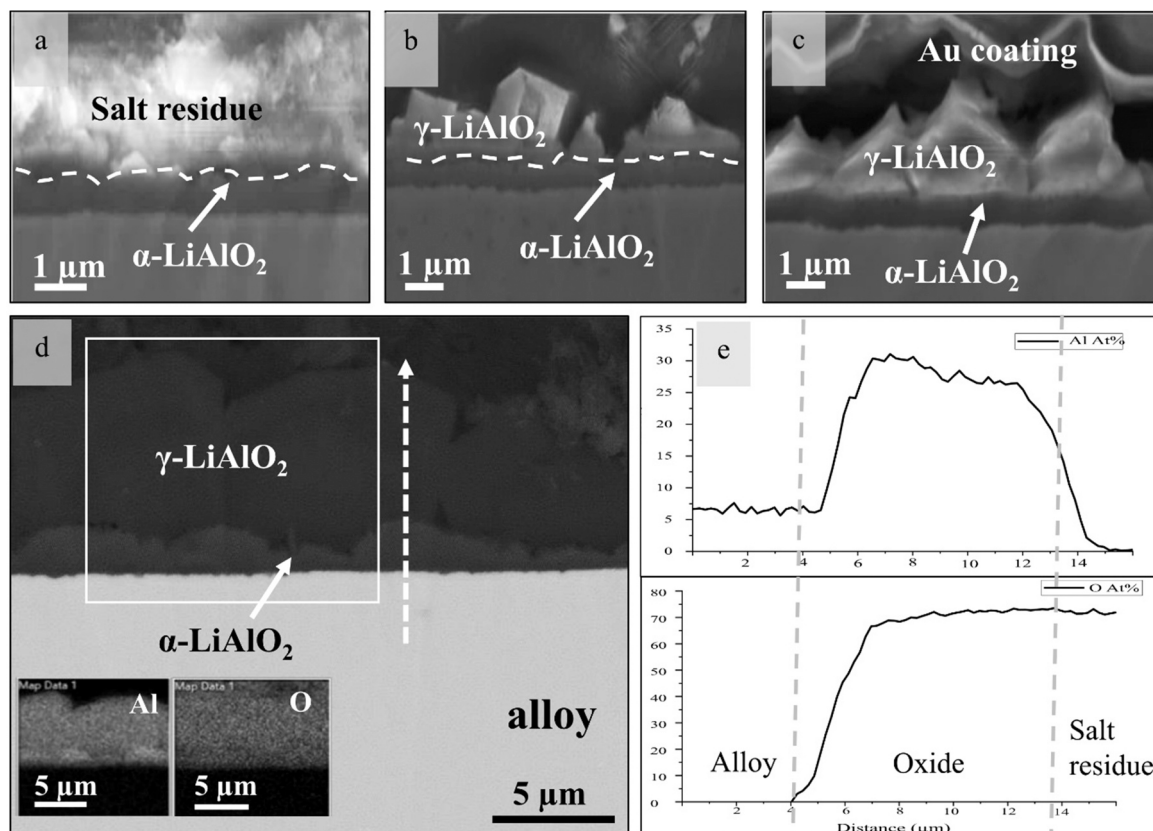


Fig. 5. Cross-section of Kanthal® EF 101 immersed in LiNaK carbonate at 800 °C after a) 72 h, b) 168 h, c) 500 h and d) 1000 h and EDS mapping of Al and oxygen through crystals, e) line scans of Al and oxygen through crystals and in the bulk alloy.

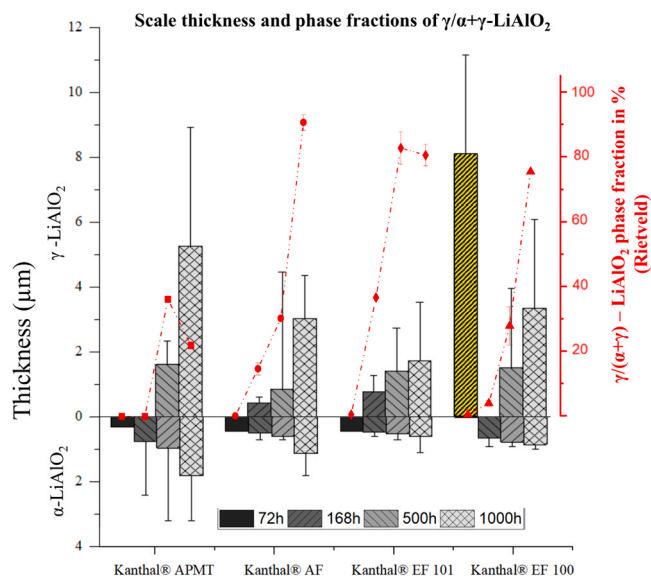


Fig. 6. Thickness values for α - and γ - LiAlO_2 of the four ferritic FeCrAl alloys and the corresponding results of Rietveld analysis, Column in yellow represents LiFeO_2 cf. Section 3.3.

and can easily leach into the alkali carbonate melt. An aluminium depletion zone in the suboxide region has been detected, reaching roughly $14\text{ }\mu\text{m}$ into the alloy. Just beneath the oxide, the aluminium content was lowered by 1.2 wt% compared to the nominal composition (see Fig. 9.f).

4. Discussion

From the experimental results, two fundamental oxidation behaviours of alumina formers in alkali carbonate melts can be distinguished. One we call the "normal" lithium aluminate formation with an initially forming inner α - LiAlO_2 and an outer γ - LiAlO_2 phase. No other cationic

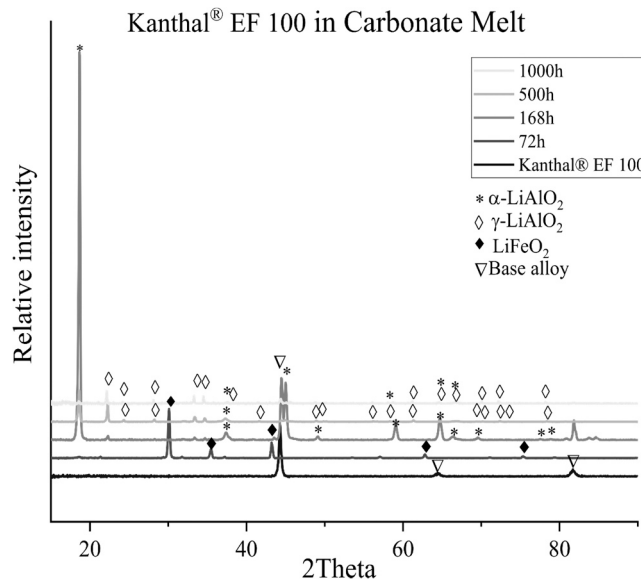


Fig. 8. XRD patterns for Kanthal® EF 100 after exposure to alkali carbonates in CO_2 at $800\text{ }^\circ\text{C}$ for 72 h, 168 h, 500 h and 1000 h.

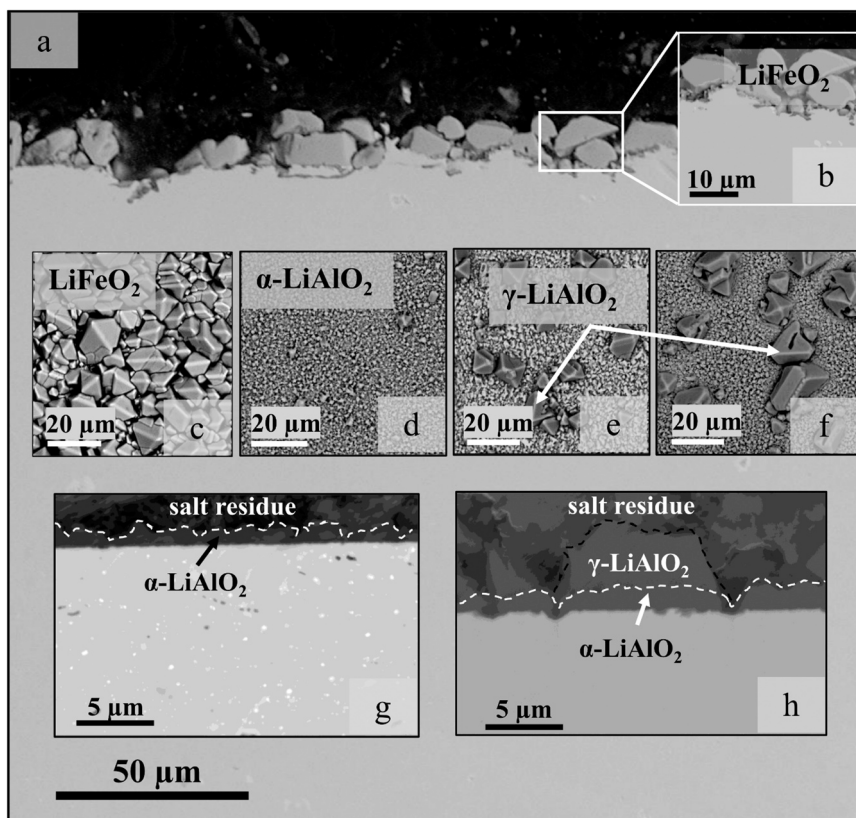


Fig. 7. Top view of Kanthal® EF 100 exposed to alkali carbonate melts at $800\text{ }^\circ\text{C}$, a, b) Cross section after 72 h. Top-view image of c) 72 h, LiFeO_2 covers the surface, d) 168 h, only α - LiAlO_2 covers the surface, e) 500 h, γ - LiAlO_2 crystallites appear, f) 1000 h, γ - LiAlO_2 crystallites size increased. Cross-section after g) 168 h, h) 1000 h.

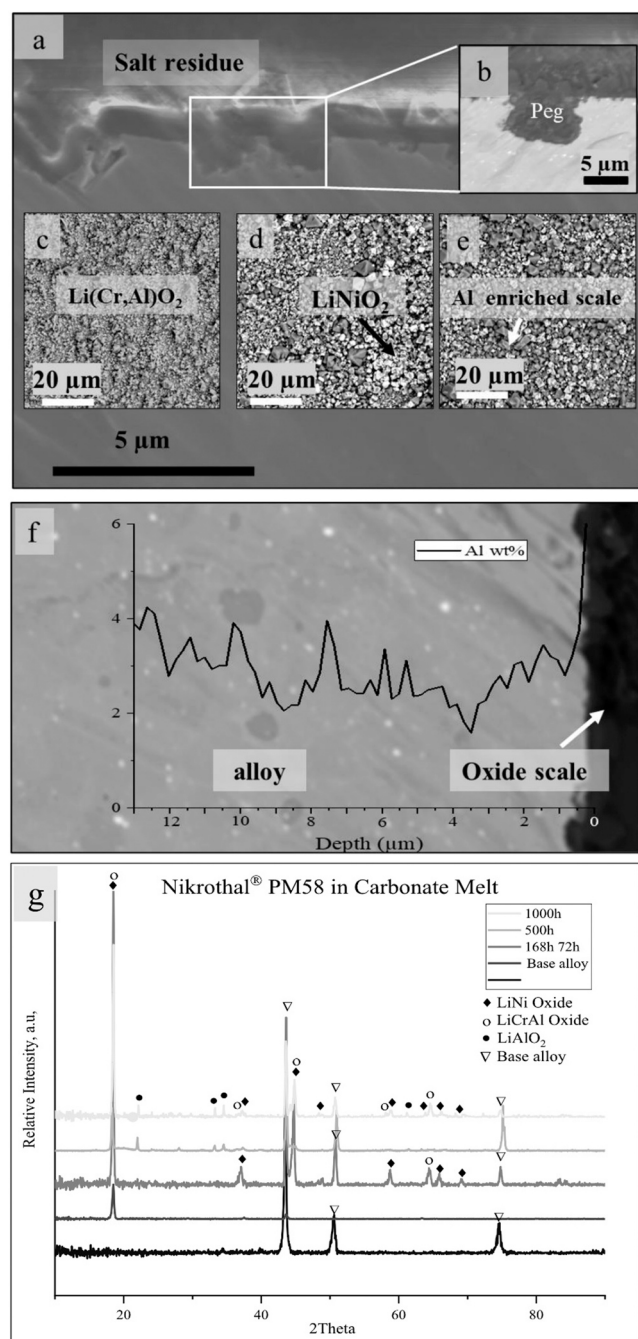


Fig. 9. Nikrothal® PM58 exposed to alkali carbonate melts at 800 °C, Cross-section after a) 1000 h in SEM contrast, b) peg after 1000 h in backscatter contrast. Top-view image after c) 72 h, $\text{Li}(\text{Cr,Al})\text{O}_2$ covers the surface, d) 500 h, presence of nickel and iron-rich particles, e) 1000 h, Al enriched scale fractions, f) line scan for the suboxide zone after 1000 h, g) XRD patterns for Nikrothal® PM58 after exposure to alkali carbonates in CO_2 at 800 °C for 72 h, 168 h, 500 h and 1000 h.

species is interfering or detected on the scale. Every other behaviour has been denominated "deviating" oxidation of alumina forming alloys in contact with alkali carbonates involving transient oxide formation and pegging.

4.1. "Normal" LiAlO_2 formation and transformation

"Normal" LiAlO_2 formation was observed for the alloys Kanthal® AF, Kanthal® APMT and Kanthal® EF 101. Exposure experiments in alkali

carbonates at 800 °C revealed formation of a covering $\alpha\text{-LiAlO}_2$ scale after 72 h. This homogeneous $\alpha\text{-LiAlO}_2$ scale protects the bulk alloy against internal oxidation and carburisation.

Worth noting, $\alpha\text{-LiAlO}_2$ is thermodynamically not favoured at 800 °C [13]; hence it is important to offer an understanding why the $\alpha\text{-LiAlO}_2$ scale is present at this temperature and grows with time. At this point, we want to remind the reader of Evans' et al. oxidation mechanism for phase stabilisation under compressive growth stress [17]. $\alpha\text{-LiAlO}_2$ has a significantly higher theoretical density compared to the γ -modification. Therefore, the growing $\alpha\text{-LiAlO}_2$ scale is able to accommodate not only a higher amount of oxygen but also lithium ions in the same volume compared to $\gamma\text{-LiAlO}_2$ and thereby absorbing growth stresses. From a corrosion control point of view, $\alpha\text{-LiAlO}_2$ is the preferential crystal morphology because it forms a dense scale that maintains a slow and gradual oxidation process.

However, in this study, we found the $\gamma\text{-LiAlO}_2$ morphology signal after 168 h in the XRD patterns for all ferritic alumina forming alloys in conjunction with larger faceted crystallites at the surface. $\gamma\text{-LiAlO}_2$ crystallites are free-standing at the melt/oxide interphase and do not experience compressive growth stresses.

The amount of both LiAlO_2 modifications increases with time, whereby $\alpha\text{-LiAlO}_2$ is the only phase initially, while $\gamma\text{-LiAlO}_2$ takes quickly over, as shown in Fig. 6. Since the formation and growth of $\alpha\text{-LiAlO}_2$ depends on the presence of compressive stresses, we, therefore, expect to find a steady-state behaviour of the inner scale. The stress relaxation will define the limiting inner α -scale thickness at the gas/oxide interface into the thermodynamically stable γ -modification. In this study, we have not reached the limiting α -scale thickness yet; however, its scale growth rate already significantly declines after 1000 h, while the γ -crystallites keep growing. Rietveld refinement also confirmed an increasing surface coverage of $\gamma\text{-LiAlO}_2$ with time.

The $\alpha\text{-LiAlO}_2$ steady-state thickness is expected to be temperature-dependent. At temperatures below 750 °C, $\alpha\text{-LiAlO}_2$ is the thermodynamically dominating morphology and therefore, $\gamma\text{-LiAlO}_2$ nucleation is unexpected.

Due to the fast growth and individual crystallinity, $\gamma\text{-LiAlO}_2$ limits the lifetime of the alloy in the melt in two ways. On the one hand, the absence of the covering $\alpha\text{-LiAlO}_2$ scale and consequently poor diffusion barrier increases accessibility of corrosion species to the metal surface. On the other hand, the faster growth of $\gamma\text{-LiAlO}_2$ crystallites accelerates the depletion of aluminium from the alloy eventually compromising the formation of a protective $\alpha\text{-LiAlO}_2$ scale.

4.2. "Deviating" LiAlO_2 formation and transformation

Two of the alumina forming alloys, Kanthal® EF 100 and Nikrothal® PM58, investigated in this study, have not shown the here called "normal" LiAlO_2 scale evolution.

As shown in the results for 800 °C, Kanthal® EF 100 presents with an external lithium ferrite, LiFeO_2 , after 72 h. After 168 h, the LiFeO_2 phase has disappeared, presumably due to dissolution, and a "normal" LiAlO_2 scale has formed and remained at least until the end of the experiment. Lacking the beneficial silicon content, Kanthal® EF 100 rapidly grows initially a covering LiFeO_2 scale. After reaching a sufficiently high thickness ($\sim 8.0 \mu\text{m}$ after 72 h), oxygen and lithium activities are low enough to nucleate a slow-growing LiAlO_2 at the metal/scale interface, decreasing the growth significantly. LiFeO_2 is leachable into the melt and has dissolved completely after 168 h. This LiAlO_2 undergoes further α -to γ -transformation as described in the former section on "normal" LiAlO_2 formation.

This result is very similar to observations made by comparing the oxidation behaviour of Kanthal® EF 100 and Kanthal® EF 101 in dry air [25].

Even though the chemical composition for both alloys is very similar, differing exclusively in silicon content, Kanthal® EF 101 grows reliably on an aluminium oxide scale in the referenced case in dry air while

Kanthal® EF 100 rapidly grows iron oxide instead [25].

Of note, the newly developed Kanthal® EF 100 and Kanthal® EF 101 have been used in former publications under names “model alloy 198” and “model alloy 197”, respectively.

The silicon contribution to the protective alumina scale formation is addressed as 3rd element effect. In our study here, the 3rd element effect of silicon as alloying element extends even beneficially for the reliable formation of α -LiAlO₂ in carbonate melts.

Nikrothal® PM58 deviates in another way from all other exposed alumina forming alloys investigated in this study. As austenitic alumina forming alloy, aluminium diffusion towards the metal/scale interface is a priori slower than for the four ferritic alloys [26], as seen in the flat aluminium profile in the suboxide region (Fig. 9.f). As described in Section 4.1. on “normal” LiAlO₂ formation, an intact α -LiAlO₂ can only be maintained by a steady-state supply of aluminium to the metal/scale interface. A covering α -LiAlO₂ scale could not be detected after exposure to alkali carbonates at 800 °C. This result strongly contrasts with an earlier study also undertaken in the same lab revealing that a protective slow-growing scale was formed and sustained at 750 °C for at least 740 h [24]. This observation indicates a strong correlation with the temperature dependence of LiAlO₂ phase transition investigated by [13], where the lower limit for γ -LiAlO₂ formation was indeed 750 °C.

5. Conclusions

All ferritic alumina forming alloys investigated in this study formed a dense and adherent α -LiAlO₂ scale after max. 168 h at 800 °C, fully immersed in alkali carbonates under flowing CO₂. This scale grows slowly and protects the alloy from internal oxidation and carburisation, which are common major corrosion problems for chromia forming high temperature alloys in contact with carbonates or CO₂.

However, the α -LiAlO₂ forms initially due to growth stress. On top of the α -LiAlO₂ scale, the thermodynamically stable γ -LiAlO₂ nucleates and rapidly grows non-protective crystals. Up to 1000 h of exposure, no detrimental aluminium depletion from the alloys was reached. The austenitic alloy Nikrothal® PM58 does not grow the preferable α -LiAlO₂ at 800 °C due to the relatively slow diffusion of aluminium from the alloy towards the alloy/melt interface.

CRedit authorship contribution statement

Esraa Hamdy: Conducting exposure experiments, sample analyses, main author of this article. **Michal Strach:** Using Rietveld refinement method, TOPAS V6 software, α/γ -LiAlO₂ phase fraction calculations, co-authoring this article. **Johanna Nockert Olovssjö:** Sample material advisor and main project partner for materials supplying at Kanthal, co-authoring this article. **Christine Geers:** Conducting exposure experiments, sample analyses, co-authoring this article.

Declaration of Competing Interest

The authors declare that they have no known competing financial interests or personal relationships that could have appeared to influence the work reported in this paper.

Data Availability

The raw/processed data required to reproduce these findings will be made available upon request. Additional data of a previous publication can be found [23].

Acknowledgements

This work was financially supported by Vinnova within the ALSTER Project as part of the Jernkontoret initiative Metalliska Material. The Swedish Energy Agency financially supported our efforts within the

thermal storage for SOLEL initiative under contract number 44653-1 (Jan-Erik Svensson) and as a partner in the High Temperature Corrosion Competence Centre (Lars-Gunnar Johansson).

References

- [1] C. Prieto, S. Fereres, F.J. Ruiz-Cabañas, A. Rodríguez-Sánchez, C. Montero, Carbonate molten salt solar thermal pilot facility: Plant design, commissioning and operation up to 700 °C, *Renew. Energy* 151 (2020) 528–541.
- [2] M. Mehos, C. Turchi, J. Vidal, M. Wagner, Z. Ma, C. Ho, W. Kolb, C. Andracka, A. Kruizenga. Concentrating Solar Power Gen3 Demonstration Roadmap, in: National Renewable Energy Lab, NREL, Golden, CO (United States, 2017.
- [3] W. Ding, A. Bonk, T. Bauer, Corrosion behavior of metallic alloys in molten chloride salts for thermal energy storage in concentrated solar power plants: A review, *Frontiers of Chemical Science and Engineering* (2018) 564–576, <https://doi.org/10.1007/s11705-018-1720-0>.
- [4] M. Liu, N.H. Steven Tay, S. Bell, M. Belusko, R. Jacob, G. Will, W. Saman, F. Bruno, Review on concentrating solar power plants and new developments in high temperature thermal energy storage technologies. *Renewable and Sustainable Energy Reviews*, Elsevier, 2016, pp. 1411–1432.
- [5] M. Walczak, F. Pineda, A.G. Fernández, C. Mata-Torres, R.A. Escobar, Materials corrosion for thermal energy storage systems in concentrated solar power plants, *Renew. Sustain. Energy Rev.* 86 (2018) 22–44.
- [6] T.D. Nguyen, J.Q. Zhang, D.J. Young, Microstructures of chromia scales grown in CO₂, *Mater. High. Temp.* 32 (1–2) (2015) 16–21.
- [7] E. Hamdy, J.N. Olovssjö, C. Geers, Perspectives on selected alloys in contact with eutectic melts for thermal storage: nitrates, carbonates and chlorides, *Sol. Energy* 224 (2021) 1210–1221.
- [8] H. Hattendorf, C.G.M. Hermse, R.M. IJzerman, The influence of alloying elements on metal dusting behavior of nickel chromium alloys and their statistical correlation, *Mater. Corros.* 70 (8) (2019) 1385–1399.
- [9] P. Szakalos, M. Lundberg, R. Pettersson, The role of discontinuous precipitation in metal dusting, *Mater. Sci. Forum* 461–464 (2004) 561–570.
- [10] M. Spiegel, P. Biedenkopf, H.J. Grabke, Corrosion of iron base alloys and high alloy steels in the Li₂CO₃-K₂CO₃ eutectic mixture, *Corros. Sci.* 39 (7) (1997) 1193–1210.
- [11] H.E. Evans, D.J. Norfolk, T. Swan, Perturbation of parabolic kinetics resulting from the accumulation of stress in protective oxide layers, *J. Electrochem. Soc.* 125 (1978) 1180–1185.
- [12] H.-A. Lehmann, H. Hesselbarth, Zur Kenntnis der Lithiumaluminate. I. Über eine neue Modifikation des LiAlO₂, *Z. für Anorg. und Allg. Chem.* 313 (1–2) (1961) 117–120.
- [13] V. Danek, M. Tarniowy, L. Suski, Kinetics of the $\alpha \rightarrow \gamma$ phase transformation in LiAlO₂ under various atmospheres within the 1073–1173 K temperatures range. *J. Mater. Sci.* 39 (2004) 2429–2435.
- [14] S.J. Heo, B. Hu, M.A. Uddin, A. Aphale, A. Hilmi, C.Y. Yuh, A. Surendranath, P. Singh, Role of exposure atmospheres on particle coarsening and phase transformation of LiAlO₂, *J. Electrochem. Soc.* 164 (8) (2017) H5086–H5092.
- [15] A. Agüero, M.C. García, R. Muelas, A. Sánchez, F.J. Pérez, D. Duday, M.P. Hierro, C. Gomez, Al slurry coatings for molten carbonate fuel cells separator plates, *High Temp. Corros. Prot. Mater.* 5 (2001) 759–766, <https://doi.org/10.4028/www.scientific.net/MSF.369-372.759>.
- [16] H.J. Choi, J.J. Lee, S.H. Hyun, H.C. Lim, Phase and microstructural stability of electrolyte matrix materials for molten carbonate, *Fuel Cells* 10 (4) (2010) 613–618.
- [17] H.E. Evans, D.J. Norfolk, T. Swan, Perturbation of parabolic kinetics resulting from the accumulation of stress in protective oxide layers, *J. Electrochem. Soc.* 125 (7) (1978) 1180–1185.
- [18] P. Bouvier, E. Djurado, G. Lucazeau, T. Le Bihan, High-pressure structural evolution of undoped tetragonal nanocrystalline zirconia, *Phys. Rev. B* 62 (13) (2000) 8731–8737.
- [19] W. Harlow, A.C. Lang, B.J. Demaske, S.R. Phillpot, M.L. Taheri, Thickness-dependent stabilization of tetragonal ZrO₂ in oxidized zirconium, *Scr. Mater.* 145 (2018) 95–98.
- [20] D.J. Spengler, A.T. Motta, R. Bajaj, J.R. Seidensticker, Z. Cai, Characterization of Zircaloy-4 corrosion films using microbeam synchrotron radiation, *J. Nucl. Mater.* 464 (C) (2015) 107–118.
- [21] K. Momma, F. Izumi, VESTA 3 for three-dimensional visualization of crystal, volumetric and morphology data, *J. Appl. Crystallogr.* 44 (6) (2011) 1272–1276.
- [22] A.-M., Lejus, Sur la formation à haute température de spinelles non stoechiométriques et de phases dérivées dans plusieurs systèmes d'oxydes à base d'alumine et dans le système alumine-nitrate d'aluminium. 1964, Masson et Cie: Paris.
- [23] E., Hamdy, J.N. Olovssjö, and C. Geers, Additional data and experimental setups used for the study on alloys in contact to high temperature eutectic melts for thermal storage 2021: Data in Brief. Revisions submitted.
- [24] E., Landberg, et al., New alumina-forming steels for future energy production with focus on solar power. 2016: Jernkontoret, Stockholm.
- [25] V. Asokan, J. Eklund, S. Bigdeli, T. Jonsson, The influence of Si on the primary protection of lean FeCrAl model alloys in O₂ and O₂+H₂O at 600 °C—A microstructural investigation, *Corros. Sci.* 179 (2021), 109155.
- [26] D.J. Young, in: D.J. Young (Ed.), Chapter 5 - Oxidation of Alloys I: Single Phase Scales, in *High Temperature Oxidation and Corrosion of Metals*, second ed., Elsevier, 2016, pp. 193–260.